Orthogonal Collocation on Finite Element Method for Driven Cavity Flow

Taejin Jang

A thesis

submitted in partial fulfillment of the

requirements for the degree of

Master of Science in Chemical Engineering

University of Washington

2017

Committee:

Venkat R. Subramainan, Chair

Qiuming Yu

Program Authorized to Offer Degree:

Chemical Engineering

University of Washington

Abstract

Orthogonal Collocation on Finite Element Method for Driven Cavity Flow

Taejin Jang

Chair of the Supervisory Committee:

Venkat R. Subramanian

Washington Research Foundation Innovation Professor of
Chemical Engineering & Clean Energy

Among the candidates feasible to be used as Electrical Energy Storage (EES), Redox Flow Batteries (RFB) is advantageous in high capacity and long lifespan. However, the study of dynamic control of RFB systems which requires fast and accurate solver for fluid dynamics is still controversial. One of the reason is that the Navier-Stokes equation does not have any known analytical solution. It explains why the numerical method, which is excellent in both accuracy and speed, is essential but is largely unavailable. Among the numerous models and cases, the most prevalent one is lid-driven cavity flow. In this study, Orthogonal Collocation on Finite Element (OCFE) method on successive subdomains is discussed from the viewpoint of accuracy and computational cost. The results show that OCFE converges as fast as other popular methods and is accurate enough to serve as a solver for the RFB simulation.

TABLE OF CONTENTS

LIST OF FIGURES

LIST OF TABLES

Chapter 1. INTRODUCTION

Electricity is the essence of the modern civilization. It is truly beneficial compared to other fossil-based fuels because they require massive transportation due to its mass and volume. Despite these benefits, conventional fossil-based fuels dominate the energy system, because electricity is not a natural energy source. This problem gets complicated considering the shifting trends from fossil-based energy to renewable energy and discrepancy in demand and supply. The feasible solution for this quest is energy storage device that is apt for each of the purposes, and it requires further study to maximize the performance.

1.1 Recent Trend

1.1.1 Trends in demand of electricity

Figure 1.1 shows the quarterly average of demands of electricity during a day in the state of California in 2016[1]. There are two distinctive patterns: one is maximum and minimum on the evening and daybreak, and another is that demand increases significantly during the night in Q3. This deviation results in huge fluctuation in the grid system and require a grid capacity large enough to prevent sudden power surges or unexpected failures in the grid system. This motivates the concept of 'reserve margin' defined by the equation [1.1].

$$\text{reserve margin} = \frac{\text{capacity - demand}}{\text{demand}} \qquad [1.1]$$

Since it is determined that the reserve margin should be greater than 15%, the capacity should be at least 115% of the peak demand over the year.[2]

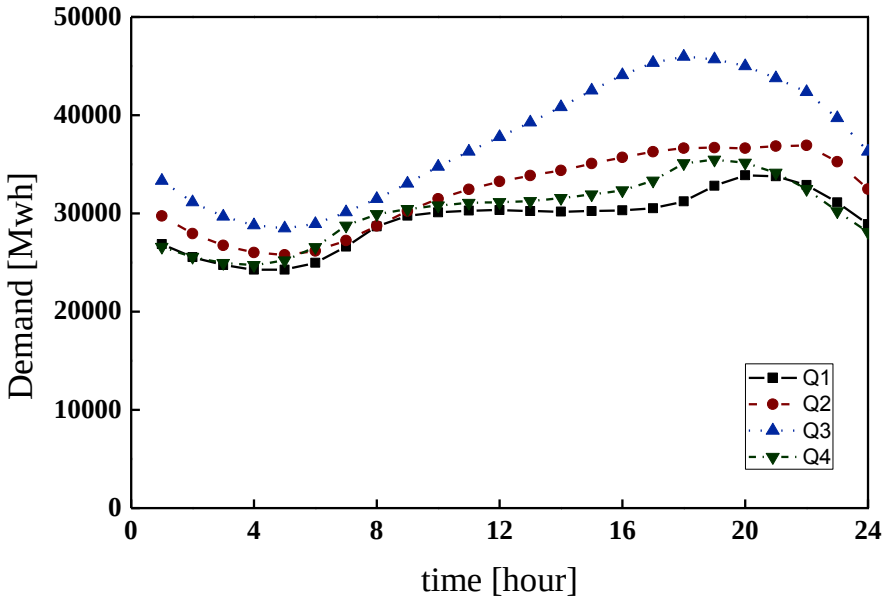

Figure 1.1. Quarterly average of demands of electricity

Meanwhile, the reserve margin greater than that means overinvestment, which is undesirable. Figure 1.2 shows the reserve margin based on an ideal capacity of 66.4 kW, which is calculated from 115% of the peak demand 57 kilowatts in July 27th, 2016[1]. This figure reveals several issues on the current grid system. The most prominent problem is the enormous reserve power from midnight to dawn. Along the day, it spikes up to 133% in Q3 and even 174% in Q1. In other words, we use only 36 to 43% of overall max capacity during midnight. The second problem is the excessive reserve margin continues over the whole days. In the evening, when the demand reaches to the peak, the margin is expected to hit the minimum, but it reached about 44% in Q3 and up to 96% in Q1. Though the high margin in Q1 may due to the less demand than Q3, but 44% of reserve margin in Q3 is due to the deviation of demands between days in Q3.

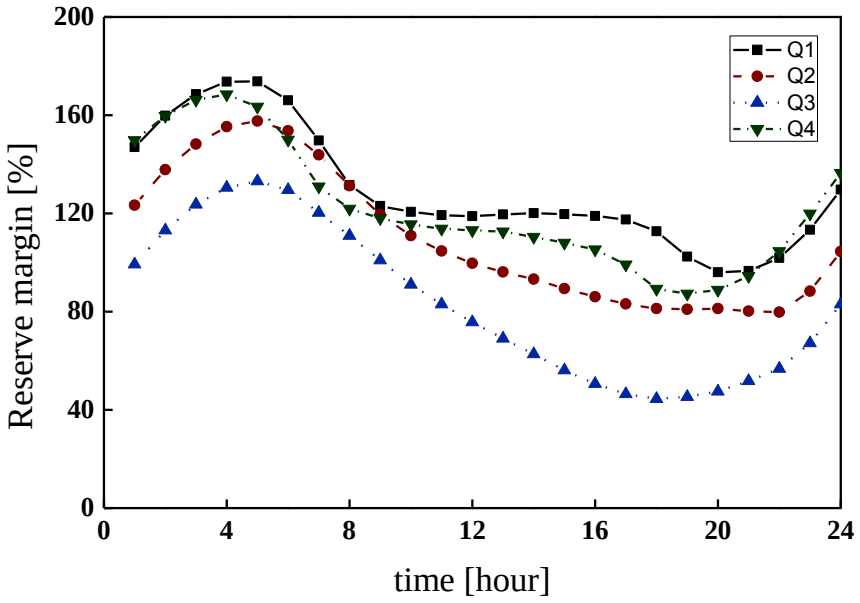

Figure 1.2. Reserve margin based on desired capacity

1.1.2 Trends in supply of electricity

One of the common strategies to mitigate the excessive reserve margin is to categorize the power plants and operate them on an as-needed basis. The first level of demands is called base load, and it determines the minimum demand of the grid. Because this kind of demand lasts 24 hours a day, the power plants and grid system which cover this load level are requested to be operative continuously. Also, low operating expenditure is expected rather than rapid respond to demands. On the contrary, there is a load level called peak demand. Most days, high demands of this level does not continue for more than a few hours, but it critically affects the reserve margin as explained in Figure 1.2. The power plants at this level do not have to be operational all day long, but it should respond to demands promptly, with a minimum delay in start-up and shut-down. Finally, there is a level between the base load and peak demand. In this level, the plants are required to be malleable

in capacity and be operational most of the day. These type of units are called load following power plants, and power plants on this level take cover the most of the fluctuation of the demand.

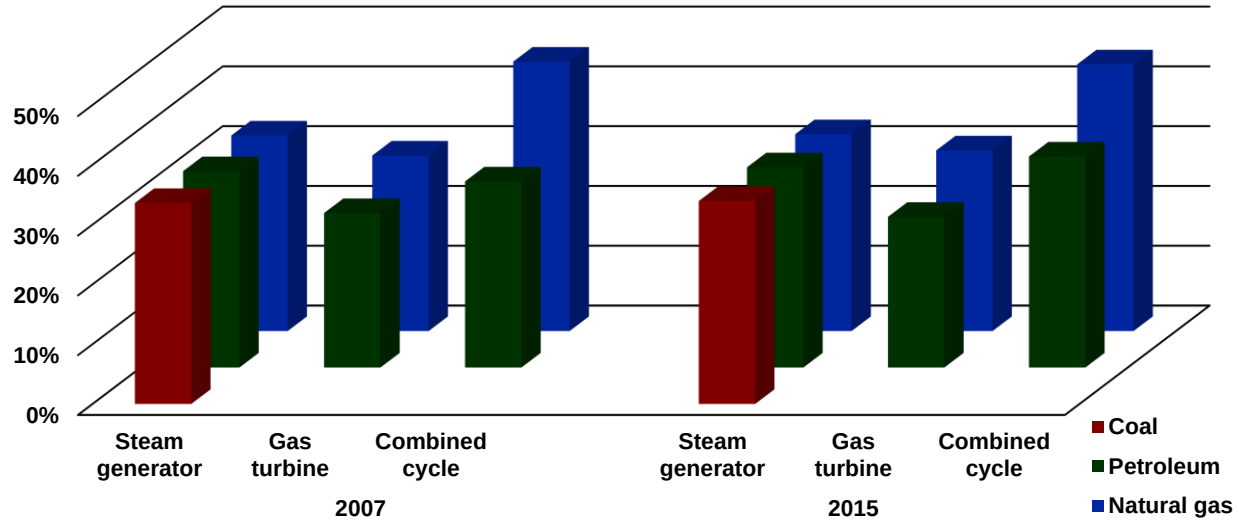

Figure 1.3. Average heat rate at full load condition

Examples of power plants for base load are nuclear and combined cycle plants with natural gas. Due to safety issue and complexity of the system, they may take a few days to reach maximum capacity and it is hard to manipulate the output swiftly. Instead, they have low fuel cost or high heat rate which results in low operating expense per unit of output. Figure 1.3 shows average heat rate of different fossil fuels and generation type at full load.[3] Among the various fuels and generation types, the combined cycle with natural gas marks the highest efficiency, approximately 45%, and ideal for base load. On the contrary, the gas turbine with natural gas is apt for peak demand loads because it needs short warm-up time to be operational. Meanwhile, the middle level of needs can be met by steam-powered power plants. Though the efficiency is not as good as steam or combined cycle, they are advantageous in the variety of fuels which leads to cost effectiveness in the fuel market.

Although we are widely using electricity in the world, there are critical problems in current grid infrastructure. The most serious one is that electricity is not an energy 'source'. The power source is defined as something that supplies more energy than we invest to get it. Even though we need to put energy to drill for the coal mines and the oil wells, the value from coal and petroleum compensates the cost and produces greater energy, just as the renewable sources like solar, wind, and geothermal do. Unlike these sources, electricity cannot be found in nature. That is why we need a generator that transforms the energy into electricity, safely and efficiently.

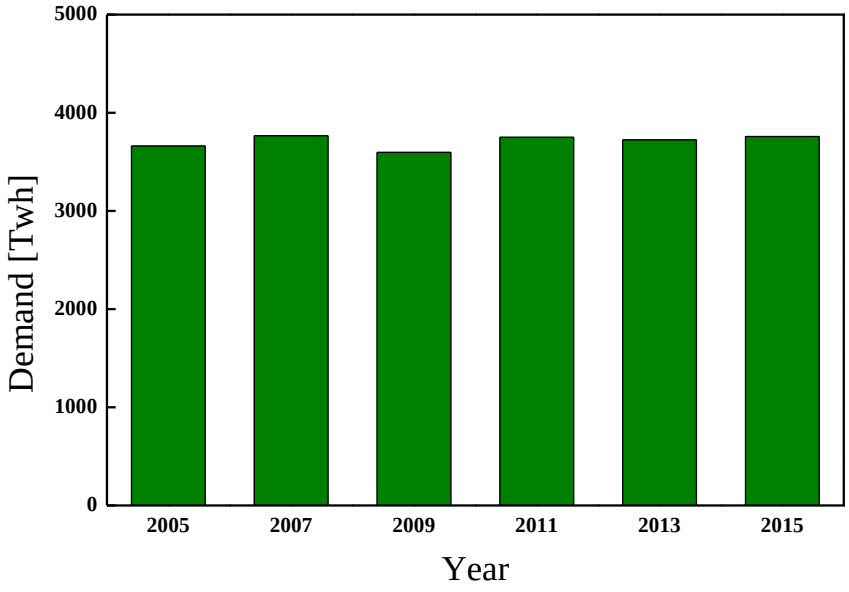

Figure 1.4. Net generation over a decade

All power plants are distinguished based on the fuel or source of energy and method to convert it to electricity. Over the years, there has been a shift of preference of the source and method of generation. Figure 1.4 shows net generation for a decade[4]. The net production was almost stagnant around 3,700 TWh. However, there were significant changes in the proportion of fuels used. As shown in figure 1.5, in the total generation by source, the share of coal has decreased by 16.5%

and most of this portion was taken by natural gas and the portion of renewable energy, increased less than 5%. This shows that the dependence on these fossil fuels has been chronic, and even worse, might continue in the future.

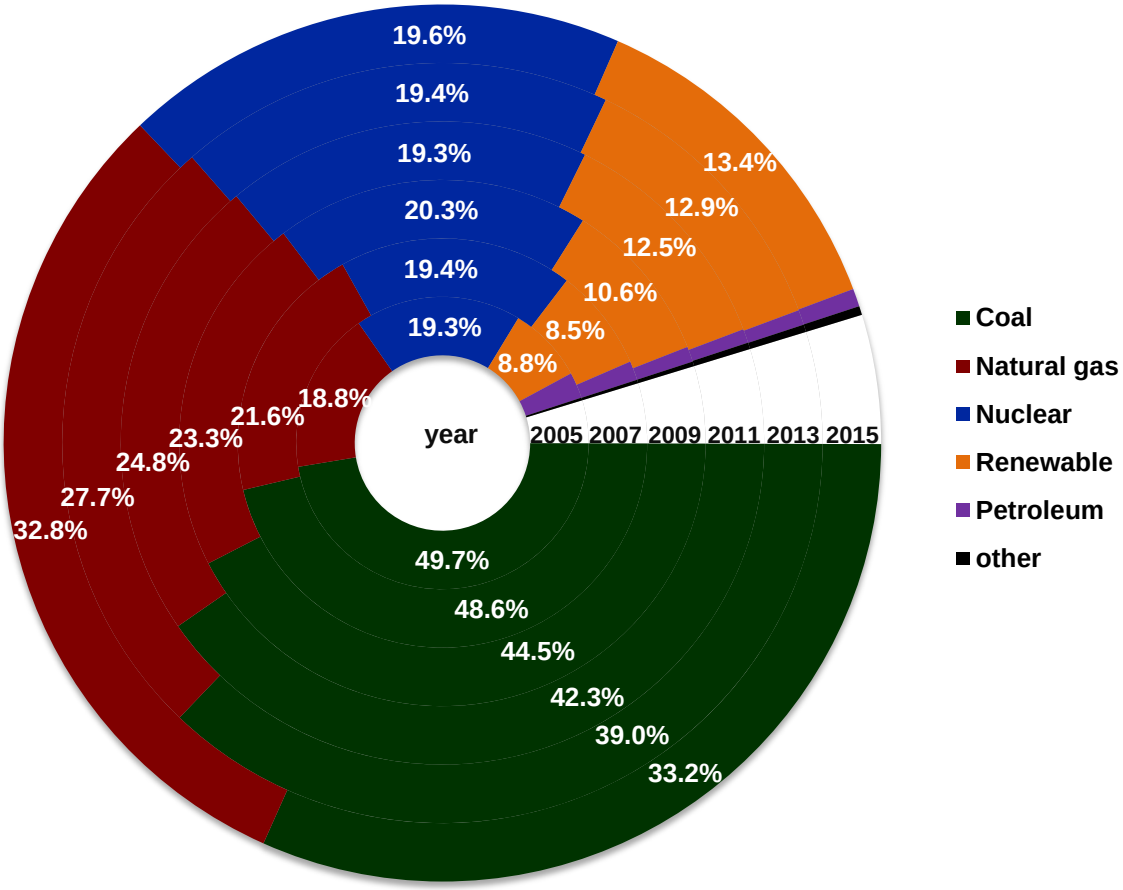

Figure 1.5. Net generation by energy sources

One feasible solution to diminish the dependency of fossil fuel is the enhancement of efficiency of conventional power plants. However, while these efforts may maintain or reduce the consumption, it cannot resolve the fundamental problem that these resources will be depleted.

1.1.3 Renewable energy

In the meantime, renewable energy, especially wind and solar, is drawing attention as alternatives. They are naturally abundant and environmentally sustainable, thus considered as an ultimate solution that fossil-based fuels cannot achieve. However, wind and solar, both promising sources of renewable energy, have fundamental problems; they are transitory and fluctuating.

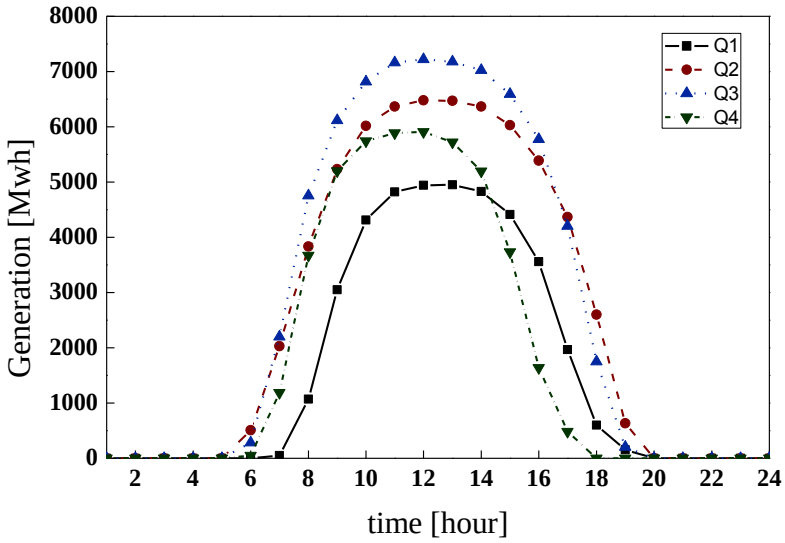

Figure 1.6. Quarterly average of solar power generation in California 2016

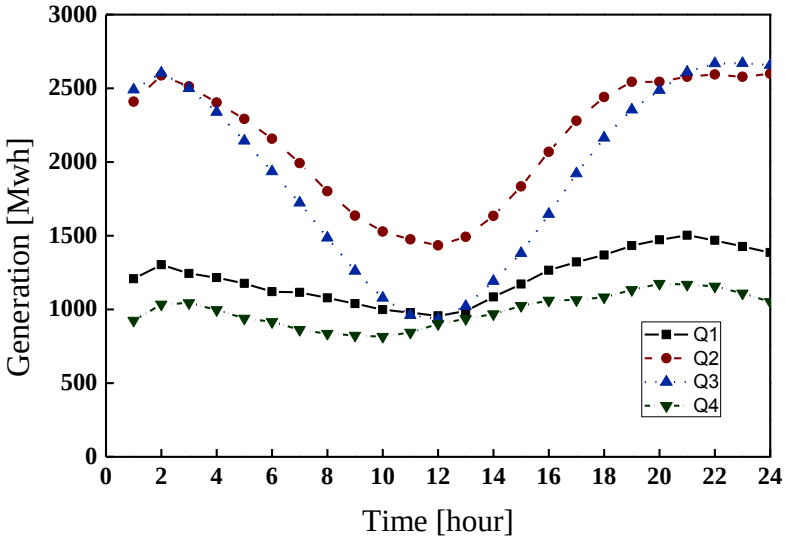

Figure 1.7. Quarterly average of wind power generation in California 2016

Figure 1.6 shows the quarterly average of solar power generation in a day in the state of California in 2016, While Figure 1.7 shows wind power in the same region and time[1]. We have sunlight during the day time and there is no output from the solar power plant after sunset. Also, it is true that we have longer daytime and stronger insolation in summer than winter and leads to higher and timely longer generation in Q2 and Q3 than Q1 and Q4. Meanwhile, wind power generation shows significant drop during day time in Q2 and Q3, and it cannot be manipulated for convenience. This trait is called transitory, and this makes hard to rely on renewable energy as the ultimate solution.

Another problem with renewable energy is the fluctuation of output due to weather. Figure 1.8 a) shows the hourly output of solar power generation in the state of California during Feb. 2016, while Figure 1.8 b) shows the wind power[1]. As mentioned earlier, there is a pattern that solar power shows high output during the day, but the absolute value is not constant over the days. Figure 1.8 a) shows the output on Feb 2nd and 17th plunged less than half of other days. Even worse, there is no pattern in wind power generation. Though the average output of wind in February was 803 MW, more than 50% of the hours in a month are even below the half of it. These data explain why we cannot consider renewable energy as an ultimate solution unless we mitigate the effects of transitory and fluctuation.

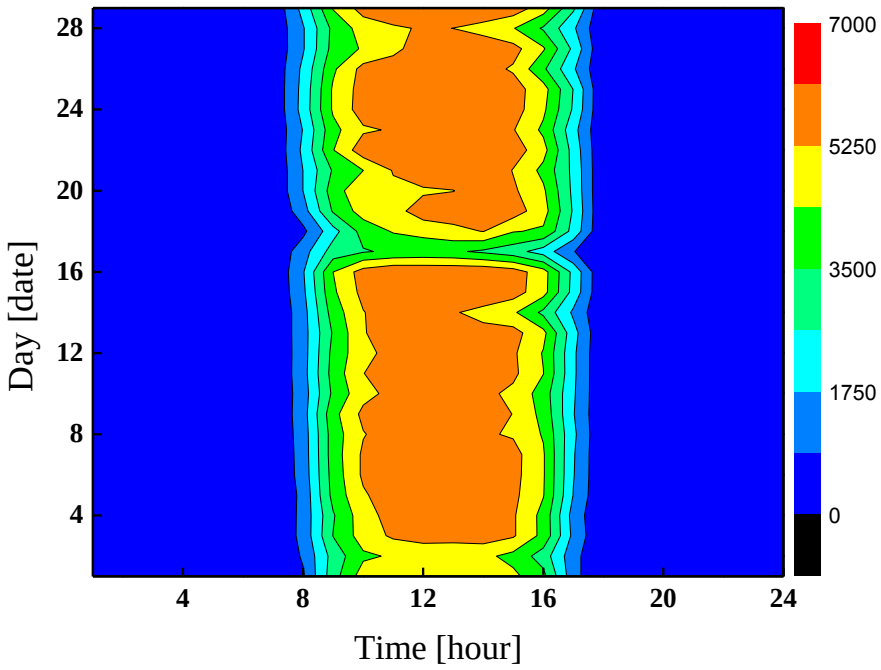

a) Hourly output of wind power generation

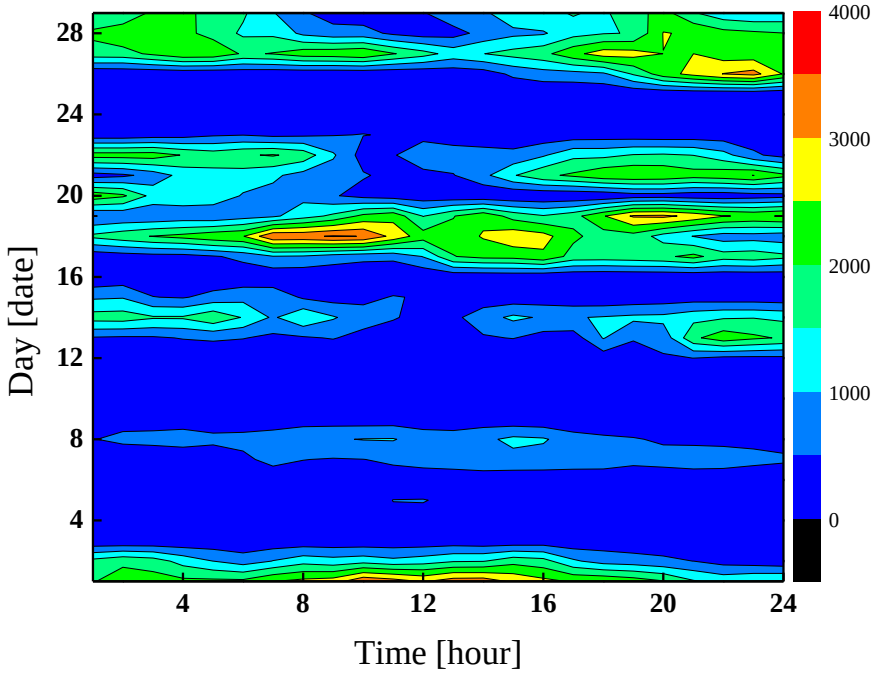

b) Hourly output of solar power generation

Figure 1.8. Hourly power generation in California Feb. 2016

1.1.4 Solutions

Dealing with these two hindrances, the high reserve margin in the conventional grid system and transitory of renewable energy, one of the feasible options is having a buffer which temporarily stores and releases electricity as needed. However, we cannot store electricity as it is. The fossil fuels are substances, and we may stock in silos or warehouses. Meanwhile, electricity is movement of electrons, and it cannot exist once the current stops. The only way we can store electrical energy is convert it to other forms.

For example, pumped hydroelectric energy storage (PHES) drains water from the reservoir and stores the energy in the form of gravitational potential. Another method is transforming the energy into chemical potential, which is happens in a battery. Though both ways are commercially available, there is a huge difference in the application. While the PHES has limitations that there are only handful of places that are apt for construction of a reservoir and has high upfront costs, batteries cost more per unit of capacity and suffer capacity loss during a cycle of charge and discharge. On the other hand, PHES has huge capacity and low price per unit, while the battery has flexibility in capacity and high energy density. With these traits, PHES is applied for part of the grid system, at a scale of MW, and batteries are used for portable devices like smartphones, laptops, and electrical vehicles.

In the meantime, new energy storage system is required for smart grid system that solves the problem of excessive reserve margin and allows integration of renewables. To achieve this, low price, flexibility, and durability of capacity are needed. As explained earlier, these are the factors that cannot be done at the same time in both conventional PHES and batteries. One of the

candidates is Redox Flow Battery (RFB), which is kind of rechargeable battery that stores the energy in the electrolyte at both electrodes.

1.2 Redox Flow Battery

Unlike other batteries, Redox Flow Battery is advantageous in both capacity loss by the cycle and price per unit of capacity. Figure 1.9 shows a schematic diagram of a redox flow battery.

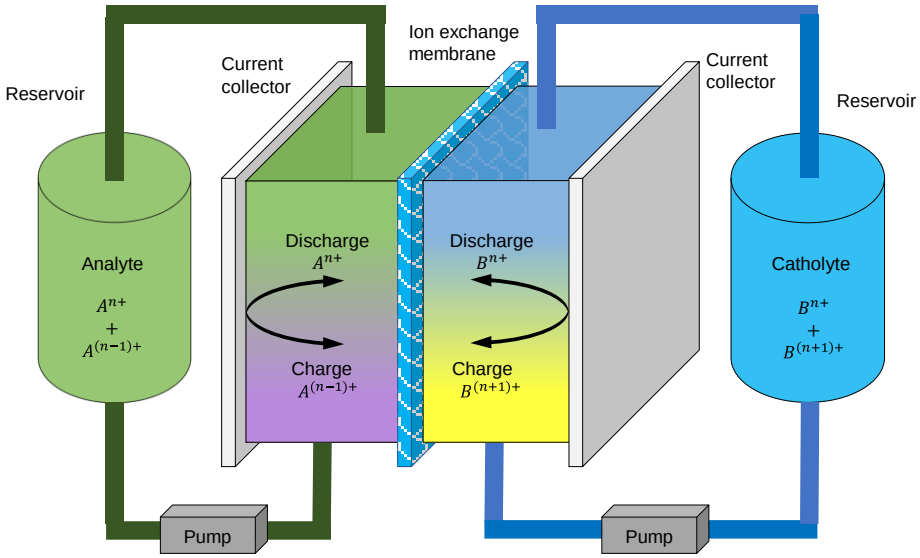

Figure 1.9. Schematic diagram of a redox flow battery

A RFB consists of electrolytes in both electrodes and a separator between them. Whereas other batteries store the energy in an electrically neutral compound, RFB stores energy in ions with following chemical equations.

$$A^{n+} + x \cdot e^{-} \underset{\text{discharge}}{\overset{\text{charge}}{\rightleftharpoons}} A^{(n-x)+} \quad \Big| \quad \text{anode} \qquad [1.2]$$

$$B^{m+} \underset{\text{discharge}}{\overset{\text{charge}}{\rightleftharpoons}} B^{(m+y)+} + y \cdot e^{-} \quad \Big| \quad \text{cathode} \qquad [1.3]$$

Instead of dissociating or associating the electron from the compounds and producing ions, electrons in a RFB interact with ions swiftly. Also, the electrolyte circulates in the reservoir and cells by a pump, and this gives good mobility to the ions and facilitates fast reaction compared to other batteries. These traits give advantages on balancing between capacity and power. While the power of the battery is proportional to the surface area of the electrode, the capacity is related to the amount of active material. For other batteries, as the amount of active material is increased, the electrodes get thicker, and the traveling distance for the charge carrier gets longer. In the end, it causes an ohmic potential drop, which leads to power loss. Also, slow reaction speed causes overpotential too. On the other hand, with good mobility and fast reaction speed, flow battery minimizes these side effects and increases the capacity by having bigger reservoir tanks that contain the electrolyte.

Unfortunately, the RFBs also have challenges to overcome. One of them is the ionic crossover. The separator between the electrolytes is an ion exchange membrane, which is for the cation to preserve electrical neutrality during charging and discharging. However, not only the cation but also the active material may cross the membrane and cause self-discharge or even worse, capacity fade. Another challenge is optimization of electrolyte flow rate. While the flow of electrolyte facilitates the reaction and minimizes the losses, it costs energy to pump the fluid and circulate it in the system. Though there have been numerous studies to find the optimal condition of flow rate

that maximizes the output, the dynamic profile is still unknown.[5] Partially, this is due to the uncertainty of parameter values, like diffusion rate or porosity of the membrane, but the ambiguity of physics of fluid dynamics can play a role in degradation of the cell components. When considering the fact that the ionic crossover is also affected by fluid dynamics, it is clear that the understanding of the motion of ions in the electrolyte and electrolyte itself is important.

Chapter 2. FLUID DYNAMICS

2.1 Governing Equations

2.1.1 Navier-Stokes equation

Like other mechanics, fluid mechanics is based on classical Newtonian physics. By the Newton's first and second law of motion, conservation of momentum can be written as follows: the D stands for material derivative and ρ, V, g, σ represent density, velocity, gravitational acceleration, and stress tensor, respectively,

$$\frac{D(\rho V)}{Dt} - \rho g - \nabla \cdot \sigma = 0 \qquad [2.1]$$

Also, consider that stress tensor can be expressed in terms of pressure p and viscous stress tensor τ, equation [2.1] is transformed into Cauchy momentum equation:

$$\frac{D(\rho V)}{Dt} = \rho g - \nabla p + \nabla \cdot \tau \qquad [2.2]$$

Though the net body force is only gravitation, the Cauchy momentum equation is valid for every dynamic fluid. However, it is impossible to get the general solution of this equation, since there is no information about the stress tensor. One of the idea is to the fluid to be a 'Newtonian fluid', i.e. the fluid or which viscous stress is proportional to deformation. With this speculation, stress tensor can be assumed as follows, with new constants μ and κ, which stand for viscosity and bulk viscosity,

$$\tau = \mu\left\{\nabla V + (\nabla V)^t\right\} + (\kappa - \frac{2}{3}\mu)(\nabla \cdot V)\delta \mid \text{Newtonian fluid} \qquad [2.3]$$

Also, we may have another simplification for the incompressible Newtonian fluid. Any-fluid should satisfy the continuity equation:

$$\frac{\partial \rho}{\partial t} + \nabla \cdot (\rho V) = \frac{\partial \rho}{\partial t} + \nabla \rho \cdot V + \rho \left(\nabla \cdot V \right) = 0 \qquad [2.4]$$

If we consider incompressible fluids, which implies that density is constant over the time domain, the partial derivative of ρ with respect to time t and gradient of ρ becomes zero, and equation [2.4] simplified as the following equation:

$$\nabla \cdot V = 0 \qquad [2.5]$$

It means that fluids should have two characteristics; constant density and divergence of velocity be zero, to be considered as incompressible. With this second element, equation [2.3] can be simplified for incompressible Newtonian fluids:

$$\tau = \mu \left\{ \nabla V + (\nabla V)^t \right\} \mid \text{incompressible Newtonian fluid} \qquad [2.6]$$

To apply this equation to Cauchy equation, we need to get the divergence of the stress tensor.

$$\nabla \cdot \tau = \nabla \cdot \mu \left\{ \nabla V + (\nabla V)^t \right\} = \mu \left\{ \nabla^2 V + \nabla (\nabla \cdot V) \right\} = \mu \nabla^2 V \qquad [2.7]$$

With implementing equation [2.7] to [2.2], the Cauchy momentum equation, we can derive Navier-Stoke's equation. Also, by implementing the explicit form of material derivative and grouping body force and pressure as a new variable P, the equation becomes:

$$\rho \left(\frac{\partial V}{\partial t} + V \cdot \nabla V \right) = -\nabla \mathrm{P} + \mu \nabla^2 V \qquad [2.8]$$

2.1.2 Vorticity

There are three basic motions in fluid; dilatation, shear, and rotation. In two dimensions, each motion is as illustrated in Figure 2.1. The dilatation is the expansion of the volume, and it contains deformation, inevitably. Shear does not involve the volumetric change, but it causes deformation. On the other hand, rotation does not have volumetric or shape change, only a change of direction. This character makes a difference when we describe the relative motion of fluids.

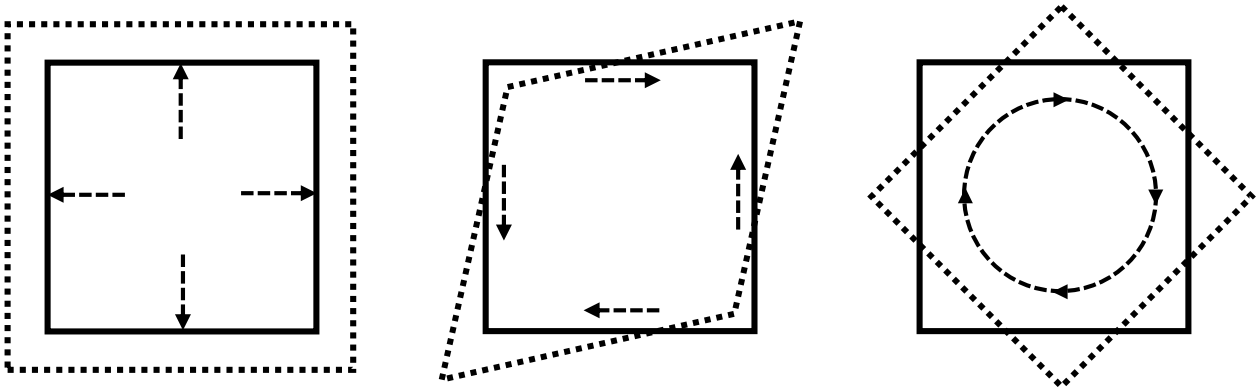

(a) Dilatation (b) Share (c) Rotation

Figure 2.1. Schematic of basic motion in fluids

In the materials in motion, including fluids, the velocity V at point r can be written as $V(r)$, and velocity at adjacent point which is apart from r by Δr, we can write it as $V(r+\Delta r)$. Between these two points, $V(r+\Delta r)$ and $V(r)$, relative velocity ΔV is defined as follows

$$\Delta V = V(r+\Delta r) - V(r) \qquad [2.9]$$

Meanwhile, $V(r+\Delta r)$ can be expressed as infinite series from Taylor expansion:

$$V(r+\Delta r)=V(r)+\Delta r\cdot\nabla V(r)+\frac{1}{2!}(\Delta r)^2:\nabla\nabla V(r)+\cdots \quad [2.10]$$

When only the first derivative term is considered and the rest of higher order terms are neglected, it can simplify the equation [2.9]:

$$\Delta V=V(r)+\Delta r\cdot\nabla V(r)-V(r)=\Delta r\cdot\nabla V(r) \quad [2.11]$$

Simultaneously, there is another relationship between relative speed Δv and the distance between two points $|\Delta r|$.

$$\Delta V(r)\cdot\Delta r=\frac{d(\Delta r)}{dr}\cdot\Delta r=\frac{1}{2}\frac{d|\Delta r|^2}{dr}=|\Delta r|\frac{d|\Delta r|}{dr} \quad [2.12]$$

Combining these two equations, another relationship can be induced:

$$|\Delta r|\frac{d|\Delta r|}{dr}=\Delta r\cdot\nabla V(r)\cdot\Delta r \quad [2.13]$$

When this equation is divided by $|\Delta r|^2$, it reveals more clear meaning:

$$\frac{1}{|\Delta r|}\frac{d|\Delta r|}{dr}=\frac{\Delta r}{|\Delta r|}\cdot\nabla V(r)\cdot\frac{\Delta r}{|\Delta r|} \quad [2.14]$$

The left-hand side stands for the rate of relative instantaneous change, which is the rate of strain. This equation clarifies that $\nabla V(r)$ is the key of strain and can be decomposed as symmetric and anti-symmetric part. It can be done by adding or subtracting the transpose of $\nabla V(r)$.

$$\nabla V(r)=\nabla V=\Gamma+\Omega \quad [2.15]$$

$$\Gamma\equiv\frac{1}{2}\left\{\nabla V+(\nabla V)^t\right\}\ \mid\ \text{symmetric} \quad [2.16]$$

$$\Omega \equiv \frac{1}{2}\left\{\nabla V - (\nabla V)^t\right\} \mid \text{anti-symmetric} \qquad [2.17]$$

An essential trait of the anti-symmetric tensor Ω is that the following equation is valid with any kind of vector a.

$$a \cdot \Omega \cdot a = 0 \qquad [2.18]$$

With this trait, it is confirmed that rate of strain depends on the symmetric part only, as the following equation, the combination of equations [2.14] and [2.15]:

$$\frac{1}{|\Delta r|}\frac{d|\Delta r|}{dr} = \frac{\Delta r}{|\Delta r|}\cdot(\Gamma+\Omega)\cdot\frac{\Delta r}{|\Delta r|} = \frac{\Delta r}{|\Delta r|}\cdot\Gamma\cdot\frac{\Delta r}{|\Delta r|} + \frac{\Delta r}{|\Delta r|}\cdot\Omega\cdot\frac{\Delta r}{|\Delta r|} = \frac{\Delta r}{|\Delta r|}\cdot\Gamma\cdot\frac{\Delta r}{|\Delta r|} \qquad [2.19]$$

As described in Figure 2.1, only the rotation does not account the deformation. It means that anti-symmetric tensor Ω takes part in describing the motion of rotation, while symmetric tensor Γ takes part in deformation. Additionally, Ω can be reformulated as follows, while ε is the alternating unit tensor:

$$\Omega \equiv \frac{1}{2}\left\{\nabla V - (\nabla V)^t\right\} = \frac{1}{2}\left\{\varepsilon\cdot(\nabla\times V)\right\} = \frac{1}{2}(\varepsilon\cdot w) \qquad [2.20]$$

This equation defines the new variable, the vorticity w.

$$w = \nabla \times V \qquad [2.21]$$

2.2 Cavity Flow

Although there is no analytical solution for the Navier-Stokes equation, approximated solution is valid with a margin of error, calculated from numerical methods.[6-9] To compare the approximated

solution with real data and estimate the accuracy, good models simple enough to compute in simulation, and observe in a physical experiment are needed. One of the models is the 'lid-driven cavity flow', shown in figure 2.2.

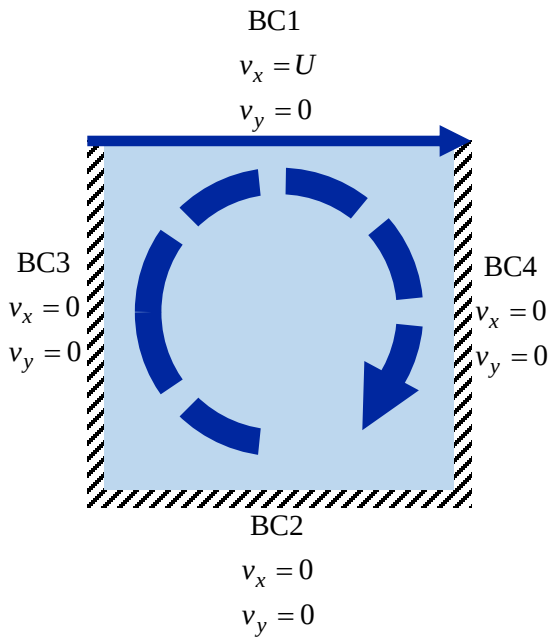

Figure 2.2. Schematic of lid-driven cavity flow and boundary condition

This model has a cavity, which is the region that is affected by the boundaries from geometry and flows. One of the simplest is a rectangular shaped cavity of length L in x and H in y axis with constant flow at the top, which is called the lid. It is called the 'lid-driven cavity flow' because the lid is the only dynamic boundary. Meanwhile, other boundaries are solid and inhibit the fluid to have zero velocity, which is called non-slip condition. One of the difficulties in the simulation of cavity flow is the discontinuity of boundaries.[10-11] There are four edges of a rectangle or square shaped hole, and two of them, located between BC1 and two solid walls, BC3 and BC4, have the discontinuity. On the solid walls in BC3 and BC4, the flow velocity in the direction of x is defined as zero, while the flow boundary BC1 has the velocity U . This overlap of two boundary conditions

mean that these edges have velocity U and zero, which is impossible. Meanwhile, if we presume that the fluid in the cavity is incompressible Newtonian, the Navier-Stokes equation can be applied to simulate the motion of the fluid. Additionally, the simulation can be simplified with square-shaped geometry and constant lid flow. In square geometry, the length L to height H is same as 1:1 and number of constants can be reduced. And the steady flow on the lids eliminate the time dependence, and it stands that time derivative of velocity is zero. With these two conditions, Navier-Stokes equation can be summarized with new constant, The Reynolds number Re:

$$\mathrm{Re}\left(\bar{V}\cdot\bar{\nabla}\bar{V}\right)=-\bar{\nabla}\bar{\mathrm{P}}+\bar{\nabla}^{2}\bar{V} \qquad [2.22]$$

$$\mathrm{Re}=\frac{\rho UL}{\mu} \qquad [2.23]$$

Though the character of the cavity flow depends on two parameters, length of the square L and boundary velocity in the x direction U, these two parameters and other constants, ρ and μ are included in Reynolds number as defined as equation [2.23]. Because the Reynolds number is the only constant in the equation, now it characterizes the dynamics of the fluids and finally the whole problem become 2D Boundary Value Problem (BVP). As a prevalent model for the testing solvers and algorithms, it has been studied with various methods and the experiment data validated the results.[12-16] Ever since Thom discussed Finite Difference Method (FDM) and ghost grid for the fluid dynamics, Woods and others implemented and expanded the method to evaluate the vorticity at the boundaries and get the solution.[17-20] Meanwhile, Finite Element Method (FEM) was discussed in earnest by Tuann and Olson.[21-24]. In conventional FEM for PDE problems, spatial discretization build the grid and defines unknown variables at each of points, and the trial function passes through these grid points. As the mesh of grid gets finer, the order of trial function gets higher and the solution becomes more accurate. Though the FEM is favorable when interpolating

the values located between the grid points, higher order of trial function demands high-performance computing with ample memory. To alleviate these cost, numerical methods which can reduce the requirement has studied, and Orthogonal Collocation on Finite Element (OCFE) method is one of them. By dividing the whole space into successive subdomains and specifying the coordinates of the points in there, it dissociate the size of the mesh and order of trial function. It successfully demonstrated that high accuracy can be achieved simultaneously with minimum number of points.[25-27]

In this study, OCFE is introduced for the cavity flow problem with imaginary points outside of the cavity. The imaginary points helps to evade the singularity points at the corner and to deduce non-flux condition and velocity profile at the boundary. The performance of the method will be discussed in the view point of accuracy and computational speed.

Chapter 3. METHOD

3.1 Governing Equation

One of the best ways to describe 2-dimensions is introducing the stream function ψ. It is defined as a contour line which is perpendicular to the velocity at each axis and gives additional benefits in visualization. Since it is valid for incompressible fluid only, it automatically satisfies the continuity condition. And the velocity in x and y direction, u and v, can be described in terms of stream function as follows:

$$u \equiv \frac{\partial \psi}{\partial y} \quad [3.1]$$

$$v \equiv -\frac{\partial \psi}{\partial x} \quad [3.2]$$

In the meantime, the motion of 2-dimentional incompressible Newtonian fluid can be described as Navier-Stokes (N-S) equation.

$$\mathrm{Re}\left(u\frac{\partial u}{\partial x} + v\frac{\partial u}{\partial y} \right) = -\frac{\partial \bar{P}}{\partial x} + \left(\frac{\partial^2 u}{\partial x^2} + \frac{\partial^2 u}{\partial y^2} \right) \quad [3.3]$$

$$\mathrm{Re}\left(u\frac{\partial v}{\partial x} + v\frac{\partial v}{\partial y} \right) = -\frac{\partial \bar{P}}{\partial y} + \left(\frac{\partial^2 v}{\partial x^2} + \frac{\partial^2 v}{\partial y^2} \right) \quad [3.4]$$

Simultaneously, the vorticity can be expressed in terms of the stream function as well:

$$w + \frac{\partial^2 \psi}{\partial x^2} + \frac{\partial^2 \psi}{\partial y^2} = 0 \quad [3.5]$$

In addition to these governing equations, the boundary conditions of cavity flow are summarized as follows:

$$(\forall x) \wedge (y = 0) : \psi = 0,\ u = 0,\ v = 0 \ | BC1 \qquad [3.6]$$

$$(\forall x) \wedge (y = 1) : \psi = 0,\ u = U,\ v = 0 \ | BC2 \qquad [3.7]$$

$$(\forall y) \wedge (x = 0) : \psi = 0,\ u = 0,\ v = 0 \ | BC3 \qquad [3.8]$$

$$(\forall y) \wedge (x = 1) : \psi = 0,\ u = 0,\ v = 0 \ | BC4 \qquad [3.9]$$

The noticeable point in boundary conditions is the absence of the condition for pressure. Though there are pressure terms in the N-S equation, it is advantageous to eliminate them to solve equation with given boundary condition. During the elimination, equation [3.3] should be differentiated by y, while [3.4] differentiated by x. It results in third order partial derivative of u and v. Consider the fact that velocity in both directions is first order derivative of stream function, the N-S equation without pressure term becomes a fourth order Partial Differential Equation (PDE). Therefore, it is beneficial to modify the N-S equation into second order partial differential of vorticity, to avoid complexity in high order derivative term:

$$\mathrm{Re} \cdot \left(\frac{\partial w}{\partial x}\frac{\partial \psi}{\partial y} - \frac{\partial w}{\partial y}\frac{\partial \psi}{\partial x} \right) - \frac{\partial^2 w}{\partial x^2} - \frac{\partial^2 w}{\partial y^2} = 0 \qquad [3.10]$$

3.2 Discretization and Grid

Conventional multi-grid methods discretize the domain along the axes and build grid points. In FEM, the solution is defined as a function which passes through these points. As the mesh of grid gets finer, the solution becomes more accurate. In return, the order of trial function also increases

proportionally and demands high computational cost. Figure 3.1 illustrate the schematic diagram of discretization where both number of stage N_{stage} and number of node N_{node} is 2. In this study, the entire domain is equally divided into $N_{stage} \times N_{stage}$ subdomains in along x and y axis, and is drawn as a solid line. To identify each of the subdomains, notation $[I, J]$ will be used. In the notation, I and J stands for index of each stage in x and y direction, from 1 to N_{stage}. Because the both axes are scaled to 1, the step size h is defined as follows:

$$h = \frac{1}{N_{stage}} \qquad [3.11]$$

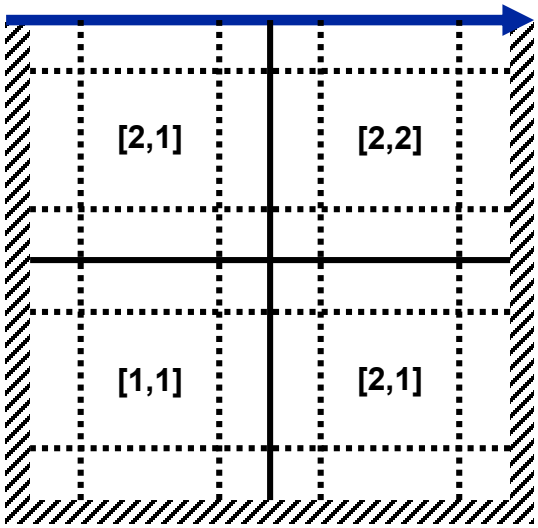

Figure 3.1. Schematic diagram of first and second discretization

Similarly, the second procedure discretizes each sub-domain into $N_{node} \times N_{node}$ grid points, drawn as dashed line. However, unlike the first time, the second discretization is conducted at roots of shifted Legendre polynomials, corresponding to the order of N_{node}. The orthogonal collocation approach with shifted Legendre polynomial guarantee the accuracy to the trial functions. The

collection of low order trial functions from the successive sub-domains can substitute high order single trial functions with accuracy and simplicity.

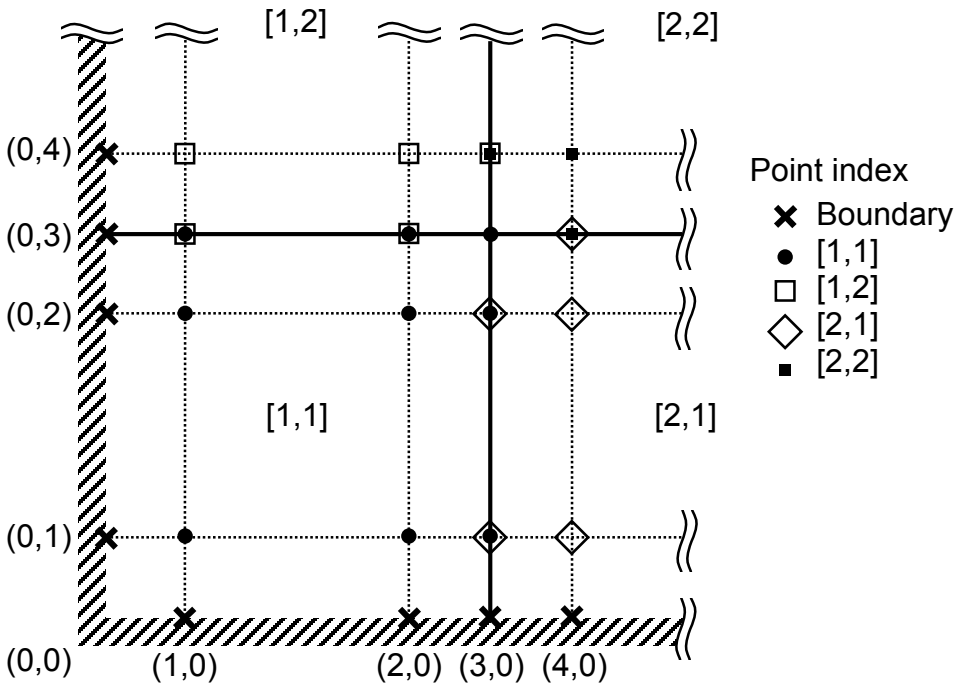

Figure 3.2. Schematic diagram of sub-domain interface

Figure 3.2 shows a schematic drawing of grid points and the boundary of subdomains at the left-bottom of the cavity, when N_{node} is 2. Each point is noted as (x_i, y_j),while i, j stands for the index of x and y axis from 0 to $(N_{node}+1)\cdot N_{stage}$. In total, there are $((N_{node}+1)\cdot N_{stage}+1)^2$ of grid points exist in the cavity. Though there are $(N_{node}+2)^2$ points in the each of subdomains, $4\bullet(N_{node}+1)$ points locate at the boundaries are shared with contiguous domain or cavity wall, and four points exist at the corners. These points which are located at the boundary or corner of

subdomains are governed by the continuity condition between subdomains, or dominated by the boundary condition.

At the subdomain $[1,1]$, a polynomial that passes through the points $\psi(x_0, y_0)$, $\psi(x_1, y_0)$, $\psi(x_2, y_0)$ and $\psi(x_3, y_0)$ is expressed as Lagrange interpolating polynomials $p(x, y_0)$, as follows.

$$p(x, y_0)_{[1,1]} = \sum_{m=0}^{3} \left(\psi(x_m, y_0) \prod_{\substack{i=0 \\ i \neq m}}^{3} \frac{x - x_i}{x_m - x_i} \right) \tag{3.12}$$

Or explicitly as,

$$\begin{aligned} p(x, y_0)_{[1,1]} = {} & \frac{(x-x_1)(x-x_2)(x-x_3)}{(x_0-x_1)(x_0-x_2)(x_0-x_3)} \psi(x_0, y_0) + \frac{(x-x_0)(x-x_2)(x-x_3)}{(x_1-x_0)(x_1-x_2)(x_1-x_3)} \psi(x_1, y_0) \\ & + \frac{(x-x_0)(x-x_1)(x-x_3)}{(x_2-x_0)(x_2-x_1)(x_2-x_3)} \psi(x_2, y_0) + \frac{(x-x_0)(x-x_1)(x-x_2)}{(x_3-x_0)(x_3-x_1)(x_3-x_2)} \psi(x_3, y_0) \end{aligned} \tag{3.13}$$

Similarly, the stream function $\psi(x, y)$ in $[1,1]$ can be expressed as a Lagrange polynomial.

$$\psi(x, y)_{[1,1]} = \sum_{n=0}^{3} \left(\left(\sum_{m=0}^{3} \left(\psi(x_m, y_n) \prod_{\substack{i=0 \\ i \neq m}}^{3} \frac{x - x_i}{x_m - x_i} \right) \right) \cdot \prod_{\substack{j=0 \\ j \neq n}}^{3} \frac{y - y_j}{y_n - y_j} \right) \tag{3.14}$$

Likewise, vorticity $\psi(x, y)$ is described by following equation:

$$w(x, y)_{[1,1]} = \sum_{n=0}^{3} \left(\left(\sum_{m=0}^{3} \left(w(x_m, y_n) \prod_{\substack{i=0 \\ i \neq m}}^{3} \frac{x - x_i}{x_m - x_i} \right) \right) \cdot \prod_{\substack{j=0 \\ j \neq n}}^{3} \frac{y - y_j}{y_n - y_j} \right) \tag{3.15}$$

With these trial functions, governing equation [3.5] and [3.10] can be reformulated as Algebraic Equations (AEs) at the interior grid points of subdomain. Meanwhile, the continuity

between the trial functions should be guaranteed at the interfaces of subdomains. In figure 3.2, $\psi(x_1, y_3)_{[1,1]}$ and $\psi(x_1, y_3)_{[1,2]}$ should be equal, as $w(x_1, y_3)_{[1,1]}$ and $w(x_1, y_3)_{[1,2]}$ do. To satisfy this condition, each subdomain shares the variables at the boundaries. For example, the stream function in $[1,2]$ is similar to equation [3.14], except that the index n range from 3 to 6. Likewise, the stream function in $[2,1]$ resembles equation [3.14] while the index m ranges from 3 to 6. It gives clue about the general form of stream and vorticity in the overall the domain which guarantees the continuity:

$$\psi(x,y)_{[I,J]} = \sum_{n=N_{J-1}}^{N_J} \left(\left(\sum_{m=M_{I-1}}^{M_I} \left(\psi(x_m, y_n) \cdot \prod_{\substack{i=M_{I-1} \\ i \neq m}}^{M_I} \frac{x - x_i}{x_m - x_i} \right) \right) \cdot \prod_{\substack{j=N_{J-1} \\ j \neq n}}^{N_J} \frac{y - y_j}{y_n - y_j} \right) \qquad [3.16]$$

$$w(x,y)_{[I,J]} = \sum_{n=N_{J-1}}^{N_J} \left(\left(\sum_{m=M_{I-1}}^{M_I} \left(w(x_m, y_n) \cdot \prod_{\substack{i=M_{I-1} \\ i \neq m}}^{M_I} \frac{x - x_i}{x_m - x_i} \right) \right) \cdot \prod_{\substack{j=N_{J-1} \\ j \neq n}}^{N_J} \frac{y - y_j}{y_n - y_j} \right) \qquad [3.17]$$

and,

$$\begin{matrix} M_I = 3 \cdot I \\ N_J = 3 \cdot J \end{matrix} \Bigg| \begin{pmatrix} \text{I}=[1\ ,\ N_{stage}] \\ \text{J}=[1\ ,\ N_{stage}] \end{pmatrix} \qquad [3.18]$$

With this general form, $4 \cdot (N_{stage})^2$ of interior grid points can be defined and converted to AEs.

In addition, smoothness of the solution at the interface should be considered. At the interface between $[I, J]$ and $[I, J+1]$, the derivative to x should match, while the sameness of derivative to the y direction is required between $[I, J]$ and $[I+1, J]$. This relationship gives another continuity condition at the interfaces, as follows:

$$\frac{\partial \psi(x,y)_{[I,J]}}{\partial x} - \frac{\partial \psi(x,y)_{[I+1,J]}}{\partial x} = 0 \;\Bigg|\; \begin{matrix} x = X \\ y = Y \end{matrix} \qquad [3.19]$$

$$\frac{\partial \psi(x,y)_{[I,J]}}{\partial y} - \frac{\partial \psi(x,y)_{[I,J+1]}}{\partial y} = 0 \;\Bigg|\; \begin{matrix} x = X \\ y = Y \end{matrix} \qquad [3.20]$$

$$\frac{\partial w(x,y)_{[I,J]}}{\partial x} - \frac{\partial w(x,y)_{[I+1,J]}}{\partial x} = 0 \;\Bigg|\; \begin{matrix} x = X \\ y = Y \end{matrix} \qquad [3.21]$$

$$\frac{\partial w(x,y)_{[I,J]}}{\partial y} - \frac{\partial w(x,y)_{[I,J+1]}}{\partial y} = 0 \;\Bigg|\; \begin{matrix} x = X \\ y = Y \end{matrix} \qquad [3.22]$$

where,

$$\begin{matrix} X = x_{M+3\cdot(I-1)} \\ Y = y_{N+3\cdot(J-1)} \end{matrix} \;\Bigg|\; \begin{matrix} I = [1, N_{stage}] \\ J = [1, N_{stage}] \\ M = [1,2] \\ N = [1,2] \end{matrix} \qquad [3.23]$$

These equations define $4\cdot\left(N_{stage}-1\right)\cdot N_{stage}$ of points on the boundaries of subdomains. Finally, the smoothness should be maintained at the junction points between four subdomains. In [1,1], two equations can be derived from both x and y direction in $\psi(x_3, y_3)$.

$$\frac{\partial \psi(x,y)_{[1,1]}}{\partial x} - \frac{\partial \psi(x,y)_{[2,1]}}{\partial x} = 0 \;\Bigg|\; \begin{matrix} x = x_3 \\ y = y_3 \end{matrix} \qquad [3.24]$$

$$\frac{\partial \psi(x,y)_{[1,1]}}{\partial x} - \frac{\partial \psi(x,y)_{[1,2]}}{\partial x} = 0 \;\Bigg|\; \begin{matrix} x = x_3 \\ y = y_3 \end{matrix} \qquad [3.25]$$

Instead of introducing two equations independently, a sum of these two equations will define the character of the grid point:

$$\left(\frac{\partial \psi (x,y)_{[1,1]}}{\partial x} - \frac{\partial \psi (x,y)_{[2,1]}}{\partial x} \right) + \left(\frac{\partial \psi (x,y)_{[1,1]}}{\partial x} - \frac{\partial \psi (x,y)_{[1,2]}}{\partial x} \right) = 0 \left| \begin{matrix} x = x_3 \\ y = \ \mathrm{y}_3 \end{matrix} \right. \quad [3.26]$$

In general form, the junction points of the subdomains can be written as follows.

$$\left(\frac{\partial \psi (x,y)_{[I,J]}}{\partial x} - \frac{\partial \psi (x,y)_{[I+1,J]}}{\partial x} \right) + \left(\frac{\partial \psi (x,y)_{[I,J]}}{\partial x} - \frac{\partial \psi (x,y)_{[I,J+1]}}{\partial x} \right) = 0 \left| \begin{matrix} x = x_{3I} \\ y = \ \mathrm{y}_{3J} \end{matrix} \right. \quad [3.27]$$

$$\left(\frac{\partial w(x,y)_{[I,J]}}{\partial x} - \frac{\partial w(x,y)_{[I+1,J]}}{\partial x} \right) + \left(\frac{\partial w(x,y)_{[I,J]}}{\partial x} - \frac{\partial w(x,y)_{[I,J+1]}}{\partial x} \right) = 0 \left| \begin{matrix} x = x_{3I} \\ y = \ \mathrm{y}_{3J} \end{matrix} \right. \quad [3.28]$$

and,

$$\begin{aligned} I &= [1, N_{stage} - 1] \\ J &= [1, N_{stage} - 1] \end{aligned} \quad [3.29]$$

Over the whole domain, there are only $(N_{stage} - 1)^2$ points left in the grid, which are equivalent to junction points. Combining two equations into one reduce the number of equations and match it with number of unknown variables.

3.3 Boundary Equation

Already explained in equation [3.6] to [3.9], boundary conditions are given as stream function and velocity of x and y direction. However, governing equations at the grid are defined with stream and vorticity. To solve the equations, vorticity at the boundary needs to be clarified. Meanwhile, there are singularities at the corner of the cavity, and should be excluded. However, the stream and

vorticity, which are defined as equation [3.16] and [3.17], already involved them. To avoid this issue, stream function and vorticity at the boundaries should be reconsidered.

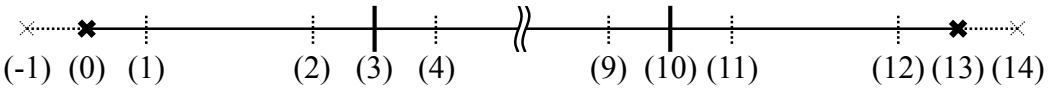

Figure 3.3. Schematic draw of ghost point in both ends

Figure 3.3 illustrates the grid points and ghost points along the x direction, when N_{node} is 2 and N_{stage} is 4. Ghost points are imaginary points locate outside of boundary, in symmetry of first inner space. With them and other $N_{node}+1$ points, stream function $\psi(x,y_J)_{[L]}$ can be defined, where $[L]$ stands the left side of the wall. In addition, the stream at the boundaries are zero and eliminate the terms which has $\psi(x_0,y_J)$ in it, and resulting in the following equation:

$$\psi(x,y_J)_{[L]}=\frac{(x-x_0)(x-x_1)(x-x_2)}{(x_{-1}-x_0)(x_{-1}-x_1)(x_{-1}-x_2)}\psi(x_{-1},y_J)+\frac{(x-x_{-1})(x-x_0)(x-x_2)}{(x_1-x_{-1})(x_1-x_0)(x_1-x_2)}\psi(x_1,y_J)+\frac{(x-x_{-1})(x-x_0)(x-x_1)}{(x_2-x_{-1})(x_2-x_0)(x_2-x_1)}\psi(x_2,y_J) \quad [3.30]$$

where,

$$x=\{x_{-1},x_0,x_1,x_2\} \quad [3.31]$$

Simultaneously, it should satisfy the velocity condition at the boundary. Because the $\psi(x,y_J)_{[L]}$ is a function of $\psi(x_{-1},y_J)$, $\psi(x_1,y_J)$, $\psi(x_2,y_J)$ and grid points along x-axis, the velocity in y direction $v(x,y_J)$, which is derivative of stream to x, gives a relationship between ghost and other two points. Meanwhile, $u(x,y_J)$ is trivial because it is a derivative of y, and $\psi(x,y_J)_{[L]}$ is not a function of y. On the other hand, considering the case that bottom and lid along y-axis

are the boundary, $u(x_I, y)$ comes to have meaning, especially the lid has non-zero condition. As a result, the velocity condition of boundaries are summarized as follows, where $[R], [D]$, and $[U]$ stand for right, bottom, and upside boundaries.

$$v(0, y_J) = \left. \frac{\partial \psi(x, y_J)_{[L]}}{\partial x} \right|_{x=0} = 0 \qquad [3.32]$$

$$v(1, y_J) = \left. \frac{\partial \psi(x, y_J)_{[R]}}{\partial x} \right|_{x=1} = 0 \qquad [3.33]$$

$$u(x_I, 0) = \left. \frac{\partial \psi(x_I, y)_{[D]}}{\partial y} \right|_{y=0} = 0 \qquad [3.34]$$

$$u(x_I, 1) = \left. \frac{\partial \psi(x_I, y)_{[U]}}{\partial y} \right|_{y=1} = 1 \qquad [3.35]$$

where,

$$\begin{aligned} I &= [1, (N_{node+1}) \cdot N_{stage} - 1] \\ J &= [1, (N_{node+1}) \cdot N_{stage} - 1] \end{aligned} \qquad [3.36]$$

With this approach, vorticity at the boundaries can be deduced. Since the boundary stream is a function of x or y only, the second derivatives to y collapse to zero at left and right boundary, while derivatives of x do at bottom and top boundary.

$$w(0, y_J) = \left. \frac{\partial^2 \psi(x, y_J)_{[L]}}{\partial x^2} \right|_{x=0} = 0 \qquad [3.37]$$

$$w(1, y_J) = \left. \frac{\partial^2 \psi(x, y_J)_{[R]}}{\partial x^2} \right|_{x=1} = 0 \qquad [3.38]$$

$$w(x_I, 0) = \left. \frac{\partial^2 \psi(x_I, y)_{[D]}}{\partial y^2} \right|_{y=0} = 0 \qquad [3.39]$$

$$w(x_I, 1) = \left. \frac{\partial^2 \psi(x_I, y)_{[U]}}{\partial y^2} \right|_{y=1} = 0 \qquad [3.40]$$

where,

$$\begin{aligned} I &= [1, (N_{node+1}) \cdot N_{stage} - 1] \\ J &= [1, (N_{node+1}) \cdot N_{stage} - 1] \end{aligned} \qquad [3.41]$$

With these boundary conditions, stream and vorticity is calculated at grid points.

Chapter 4. RESULT

As already discussed in Chapter 2, the cavity flow problem is scaled with dimension, velocity and other constants like density and viscosity. Consequently, Reynolds number characterizes the complexity of the problem. Even the cases that Reynolds number greater than 10,000 are considered to estimate the performance of the solver, the range exceeds the critical points causing a transition from laminar to turbulent flow.[28-29] In this study, the Reynolds number is limited up to 1000 and the accuracy and computational time are discussed with other algorithm and software. In OCFE method, Maple® 2016 was used, and all the simulation was conducted on the desktop with hexacore 3.4 GHz Intel® i7 CPU and 32 GB RAM.

4.1 Convergence

The common feature of numerical methods is large-scale discretization along axes, and the computational time is proportional to the scale of equations. The more relation between grid points is inaccurate, it requires finer grid and many iterations to compensate for the accuracy. In other words, as each point is correlated firmly and the order of accuracy is high, acceptable solutions are calculated in smaller grid and iteration.

Because the cavity flow problem is a BVP, the solution at the center is the most inaccurate point. When the center value matches well with the result when the grid is finer, or iteration number is greater, it guarantees that other values close to the boundaries are also accurate. Figure 4.1 a) and b) shows fluid velocity in x or y direction with OCFE, while the y or x is 0.5, respectively. When N_{stage} reaches 8, the value already starts to converge in both direction.

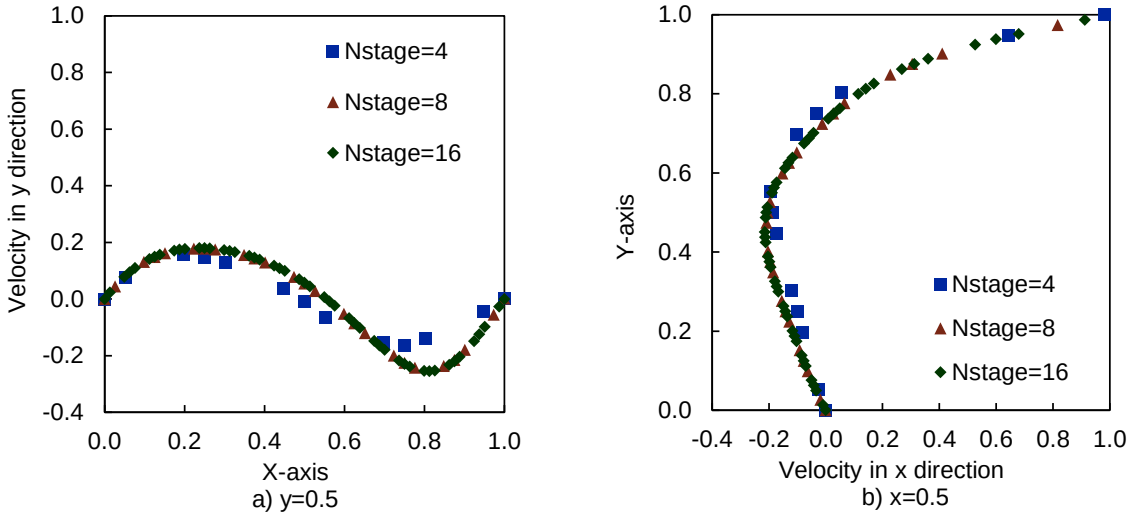

Figure 4.1. Flow velocity at the centerline while Re = 100

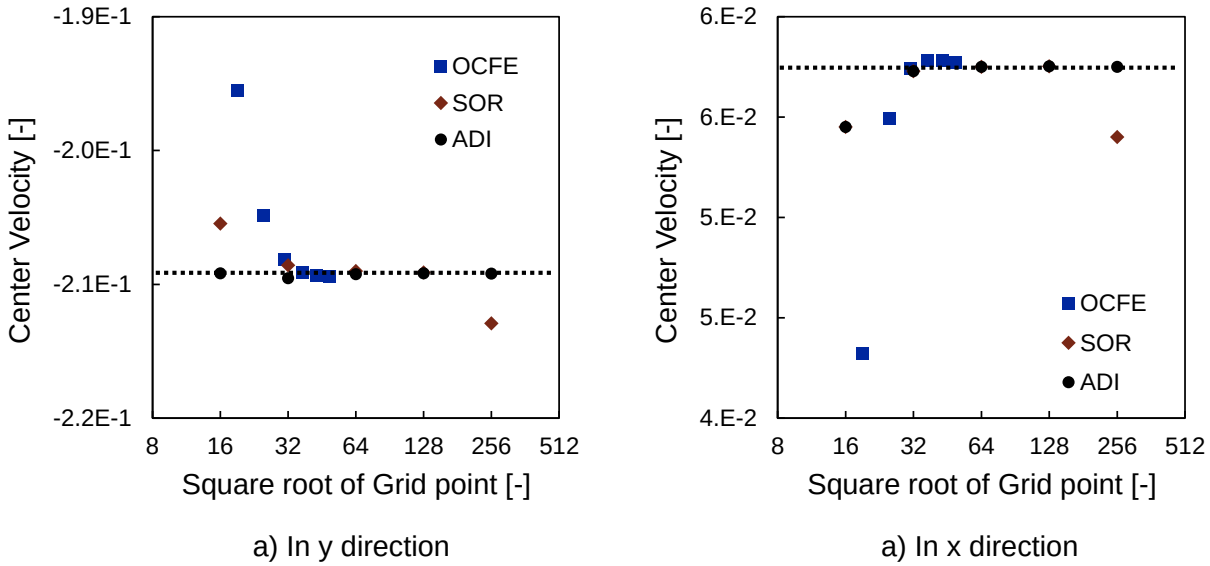

Figure 4.2. Center flow velocity in direction while Re=100

Figure 4.2 shows flow velocity in y direction, while x is 0.5. As a reference, Successive Over Relaxation (SOR), Alternating Direction Implicit (ADI) was simulated with Fortran.[30-31] Though there is no analytical solution and it is impossible to know the absolute answer, the center velocity

of OCFE and ADI in y and x direction converged to -0.209 and 0.057, respectively. However, SOR method did not converge and gave an inconclusive result.

For both SOR and ADI method, fourth order accuracy method was simulated while the OCFE guarantee minimum second order accuracy because only first order derivatives are considered at the interface between sub domains. Nevertheless, the OCFE converge as rapid as fourth order accuracy method does. It shows OCFE can achieve good convergence and accuracy with more compact equation sets. Since this simulation was performed when Reynolds number is merely 100, it will require an even large scale of grid points as Reynolds number increases. It means that OCFE is more beneficial because it requires the less computational cost in memory and time.

4.2 Computational Cost

To appraise the computational cost, OCFE is compared with SOR, ADI and COMSOL, one of the prevalent commercial software for the numerical analysis. To ensure the accuracy as references, the grid scale of SOR and ADI in Fortran was 128×128 and COMSOL was 497×497, While OCFE in MAPLE conducts the simulation with 95×95 grid. To get the solution when the Reynolds number is 400 and 1000, OCFE utilized a low Re number solution as an initial guess for the Newton-Raphson iteration.

Table 4.1. Center velocity profile in y direction on the increment of Reynolds number

Method Platform Grid Re	OCFE MAPLE 95×95	SOR Fortran 128×128	ADI Fortran 128×128	FVM COMSOL 497×497
0	-0.2052	-0.2052	-0.2052	-0.2052
100	-0.2092	-0.2092	-0.2092	-0.2093
400	-0.1152	-0.1151	-0.1151	-0.1154
1000	-0.0634	-0.0619	-0.0623	-0.0620

Table 4.1 shows the velocity in the y direction at the center (x is 0.5). For the low range of Reynolds number from 0 to 400, the solution shows consistency between all the methods. When Re was 1000, the result of OCFE was a bit different from the references, but the error was only less than 2.2%. It demonstrates that OCFE is valid even at the high Reynolds numbers.

Table 4.2. CPU time and memory usage on the increment of Reynolds number

Method Platform Grid	OCFE MAPLE 95×95		SOR Fortran 128×128		ADI Fortran 128×128		FVM COMSOL 497×497	
Re	CPU time [sec]	RAM [MB]	CPU time [sec]	RAM [MB]	CPU time [sec]	RAM [MB]	CPU time [sec]	RAM [MB]
0	40.92	173.1	1003.4	5	1300.8	5	17	1136
100	35.21	441.4	977.9	5	575.0	5	29	1843
400	55.29	441.8	992.1	5	733.8	5	50	1925
1000	62.74	498.0	993.8	5	772.4	5	60	2252

Table 4.2 shows the calculation of time and usage of RAM based on the increment of the Reynolds number. Compare to SOR and ADI, OCFE was faster, up to 27 times. Though both SOR and ADI utilized only 5 MB of memory, the benefit of improvement of time is much more valuable. On the other hand, OCFE took less memory than COMSOL, whereas COMSOL is faster or equivalent to OCFE. Though finer grid mesh in COMSOL is one of the reasons for using more resources, it was a mandatory condition to get a high accuracy close enough to the OCFE method. Also, COMSOL was optimized for the parallel computation and utilized up to 50% of CPU, while MAPLE 2015 shared only 10% of it. From the results in Table 4.1 and 4.2, OCFE method is effective in the speed of calculation and memory usage. Especially, the low usage of memory may mean that there is a possibility that finding an extremely accurate solution enough to be considered as the absolute one with limited hardware setup.

4.3 Conclusion

The RFB is the key to resolve the barrier towards the renewable energy based system. To achieve the maximum performance, the numerical solver for the optimal control is essential. In this study, the performance of the OCFE is tested with widespread 2D Cavity Flow problem. The N-S equation is mathematically reformulated to the second order PDE of stream and vorticity. The cavity is spatially discretized in two different way, one is for the subdomains, and another is for the collocation points in the each of subdomain. At the interface of the subdomains, continuity condition connects the adjacent subdomains, and help to evade the complex calculation by N-S equation. On the boundaries, the trial function is redefined with ghost points, and it circumvents the singular points at the corner of the cavity. As a result, it shows good matching with known numerical solutions, and converged fast and requires the less computational cost. Because this study conducted with MAPLE, the speed and memory usage can be improved with converting low-level language and combined with other numerical technics and solvers. Besides, it can be applied to the various field. The most promising area is optimization for the real-time control. While the conventional controller operates the system while ignoring the singularities by a sudden change of environment or mal-define of the geometry, it can minimize the effect of these problems and guarantee the robustness. Also, the low computational cost for the simulation shows another possibility. Instead of centralized control with a large scale main frame, distributed processing with inexpensive microcomputer can reduce the cost and response time simultaneously. That is why OCFE is promising and worthy to be studied and developed.

BIBLIOGRAPHY

[1] California Independent System Operator, Daily Renewables Watch, 2016. Available : http://www.caiso.com/market/Pages/ReportsBulletins/DailyRenewablesWatch.aspx

[2] U. S. Deparmtment Of Energy, *Maintaining Reliability in the Modern Power System*, 2016. p. 7.

[3] U. S. Energy Information Administration, *Electric Power Annual 2015*, 2016. p. 168.

[4] U. S. Energy Information Administration, *Electric Power Annual 2015*, 2016. p. 34.

[5] Tang, A., Bao, M., Skyllas-Kazacos, M., Studies on Pressure Losses and Flow Rate Optimization in Vanadium Redox Flow Battery. *J. Power Sourc.*, 2014. **248**: p. 154-162.

[6] Smith, A., Silvester, D., Implicity Algorithms and Their Linearization for the Transient Incompressible Navier-Stokes Equations. *IMA J. Numer. Anal.*, 1997. **17**: p. 527-545.

[7] Pironneau, O., On the Transport-Diffusion Algorithm and Its Applications to the Navier-Stokes Equations. *Numer. Math.*, 1982. **38**: p. 309-332.

[8] Oymak, O., Selcuk, N., Method-of-Lines Solution of Time-Dependent Two-Dimentional Navier-Stokes Equations. *Int. J. Numer Meth.Fluid.*, 1996. **23**: p. 455-466.

[9] Kay, D. A., Gresho, P. M., Griffiths, D. F., Silvester, D. J., Adaptive Time-Stepping for Incompressible Flow Part II: Navier–Stokes Equations. *SIAM J. Sci. Comput.*, 2010. **32**: p. 111-128.

[10] Nie, X., Robbins, M. O., Chen. S., Resolving Singular Forces in Cavity Flow: Multiscale Modeling from Atomic to Millimeter Scales. *Phys. Rev.Lett.*, 2006. **96**: p. 134501.

[11] Auteri, F., Parolini, N., Quartapelle, L., Numerical Investigation on the Stability of Singular Driven Cavity Flow. *J. Comput. Phys.*, 2002. **183**: p. 1-25.

[12] Shankar, P. N., Deshpande, M. D., Fluid Mechanics in the Driven Cavity. *Annu. Rev. Fluid Mech.*, 2000. **32**: p. 93-136.

[13] Guermond, J. L., Migeon, C., Pineau, G., Quartapelle, L., Start-up Flows in a Three-Dimensional Rectangular Driven Cavity of Aspect Ratio 1:1:2 at Re = 1000. *J. Fluid Mech.*, 2002. **450**: p. 169-199.

[14] Prasad, A. K., Koseff, J. R., Reynolds Number and End-Wall Effects on a Lid-Driven Cavity Flow. *Phys. Fluid Fluid Dynam.*, 1989. **1**: p. 208-218.

[15] Ghia, U., Ghia, K. N., Shin, C.T., High-Resolutions for Incompressible Flow Using the Navier-Stokes Equations and a Multi-Grid Method. *J. Comput. Phys.*, 1982. **48**: p. 387-411.

[16] Migeon, C., Texier, A., Pineau, G., Effects of Lid-Driven Cavity Shape on the Flow Establishment Phase. *J. Fluid Struct.*, 2000. **14**: p. 496-488.

[17] Thom, A., The Flow Past Circular Cylinders at Low Speeds. *Proc. Roy. Soc.*, 1933. **141**: p. 651-668.

[18] Woods, L. C., A Note on the Numerical Solution of Fourth Order Differnetial Equations. *Aeronautical Quarterly*, 1954. **5**: p. 176-184.

[19] Kawaguti, M., Numerical Solution of the Navier-Stokes Equations for the Flow in a Two-Dimensional Cavity. *J. Phys, Soc. Jpn.*, 1961. **16**: p. 2307-2315.

[20] Burggraf, O., Analytical and Numerical Studies of the Structure of Steady Separated Flows. *J. Fluid Mech.*, 1966. **24**: p. 113-151.

[21] Tuann, S. U., Olson, M. D., Review of Computing Methods for Recirculating Flows. *J. Comput. Phys.*, 1978. **29**: p. 1-9.

[22] Mendelson, M. A., Yeh, P. W., Brown, R. A., Armstring, R.C., Approximation Error in Finite Element Calculation. *J. Non-Newtonian Fluid Mech.*, 1982. **10**: p. 31-54.
[23] Grillet, A. M., Yang, B., Khomani, B., Shaqfeh, E. S. G., Modeling of Viscoelastic Lid Driven Cavity Flow Using Finite Element Simulations. *J. Non-Newtonian Fluid Mech.*, 1999. **88**: p. 99-131.
[24] Barragy, E., Carey, G. F., Stream Function-Vorticity Driven Cavity Solution Using P Finite Elements. *Computer & Fluids*, 1997. **26**: p. 453-468.
[25] Ferguson, N. B., Finlayson, B. A., Transient Chemical Reaction Analysis by Orthogonal Collocation. *Chem. Eng. J.*, 1970. **1**: p. 327-336.
[26] Carey, G. F., Finlsyson, B. A., Orthogonal Collocation on Finite Elements. *Chem. Eng. Sci.*, 1975. **30**: p. 587-596.
[27] Chang, P. W., Finlayson, B. A., Orthogonal Collocation on Finite Elements for Elliptic Equations. *Math. Comput. Simulat.*, 1978. p. 83-92.
[28] König. S., Suriyah, M. R., Leibfried, T., Model Based Examination on Influence of Stack Series Connection and Pipe Diameters on Efficiency of Vanadium Redox Flow Batteries under Consideration of Shunt Currents. *J. Power Sourc.*, 2015. **281**: p. 272-284.
[29] Kumar, S., Jayanti, S., Effect of Flow Field on the Performance of an All-Vanadium Redox Flow Battery. *J. Power Sourc.*, 2016. **307**: p. 782-787.
[30] E. Erturk., Discussions on Driven Cavity Flow. *Int. J. Numer. Meth. Fluids,* 2009. **60**: p. 275-294.
[31] E. Erturk., Gokcol, C., Fourth-Order Compact Formulation of Navier–Stokes Equations and Driven Cavity Flow at High Reynolds Numbers. *Int. J. Numer. Meth. Fluids,* 2006. **50**: p. 421-436.